Processing and Application of Ceramics 13 [3] (2019) 310–321
https://doi.org/10.2298/PAC1903310M



# The influence of short thermal treatment on structure, morphology and optical properties of Er and Pr doped ceria pigments: Comparative study

Dragana Mićović[1], Maja C. Pagnacco[2], Predrag Banković[2], Jelena Maletaškić[3], Branko Matović[3], Veljko R. Djokić[4], Marija Stojmenović[3,*]

[1]*Faculty of Physical Chemistry, University of Belgrade, Studentski trg 12, 11000 Belgrade, Serbia*
[2]*Institute of Chemistry, Technology and Metallurgy, University of Belgrade, Department of Catalysis and Chemical Engineering, Njegoševa 12, 11000 Belgrade, Serbia*
[3]*Vinča Institute of Nuclear Sciences, University of Belgrade, P. O. Box 522, Belgrade, Serbia*
[4]*Faculty of Technology and Metallurgy, University of Belgrade, Karnegijeva 4, 11120 Belgrade, Serbia*

Received 28 March 2019; Received in revised form 7 August 2019; Accepted 26 August 2019

## Abstract

*Potential non-toxic pink and red ceramic pigments based on $CeO_2$ were successfully synthesized by self-propagating room temperature method and thermally treated at 600, 900 and 1200 °C for 15 min. The structure, morphology and optical properties, as well as thermal stability of $Ce_{1-x}Er_xO_{2-\delta}$ and $Ce_{1-x}Pr_xO_{2-\delta}$ ($x = 0.05$) were examined. Single-phase composition of all obtained $CeO_2$ pigments was confirmed using XRPD method and Raman spectroscopy and it was not dependent on temperature. The mechanism of structural behaviour was thoroughly examined using Raman and FTIR spectroscopy. Nanometric dimensions of the crystallites of all pigments were confirmed using XRPD, TEM and FE-SEM analysis. Colour properties were dependent on the temperature treatment, and their position in the chromaticity diagram was studied using UV/VIS spectrophotometry. Colour efficiency measurements were supplemented by colorimetric analysis. It is proved that all samples are thermally stable in the investigated temperature range (up to 1200 °C), and their potential application as environmentally friendly pigments of desired colour is confirmed.*

***Keywords:*** *$CeO_2$, Er and Pr doping, structure, optical properties, colour, pigments*

## I. Introduction

Recently, almost all fields of science have been dedicated to solving different problems in order to protect the environment. One of the fields of science that deals with this problem is the field of development of new non-toxic environmentally pure inorganic pigments. Today, inorganic pigments are frequently used for the colouration of many materials in the industry including the production of plastics, ceramics, inks, rubbers, paints and glasses [1,2]. Traditional pigments, such as matrix of lead oxide ($Pb_3O_4$) and tin oxide ($SnO_2$), are used in large extents [3]. Iron oxide ($Fe_2O_3$) encapsulated in zircon ($ZrSiO_4$) matrix, which gives pale red or pink colours [3], and $Cd(S_xS_{1-x})$-$ZrSiO_4$ as red-orange pigment [4], are also widely used. However, the application of the $Cd(S_xS_{1-x})$-$ZrSiO_4$ system at temperatures above 900 °C is very toxic and unstable [4]. Although some inorganic pigments containing elements such as Pb, Sn, Fe, Cr, Se, Cd, Hg, Sb have shown excellent properties, their application is strictly controlled and regulated by legislation and regulations adopted by governments in many countries due to their high toxicity (not only for the environment but also for human health) [5–7].

Lately, many attempts have been made in order to eliminate the application of above mentioned toxic and unstable pigments [8–11]. With a few exceptions, majority of ceramic pigments is based on inorganic oxides. Researches have been increasingly focused on the development of new nanosized ceramic pigments, in particular based on cerium(IV)-oxide ($CeO_2$), with

*Corresponding author: tel: +381 11 340 8860,
e-mail: *mpusevac@vin.bg.ac.rs*

the goal of spreading the range of applications of ceramic pigments [12–15]. Thanks to their high thermal resistance, chemical stability (low corrosion) and very good optical and colouristic properties, ceramic pigments based on $CeO_2$ are increasingly used nowadays [6,7,9,10,12,13,16]. They attract particular attention because of ability to filter ultraviolet (UV) radiation and protection capabilities from the effects of solar light (UV, VIS and IR light) when applied in the form of coloured coating [13,14].

In order to enable development of environmentally non-harmful ceramic pigments based on $CeO_2$, many problems have to be solved starting with those related to powder synthesis. The syntheses of ceramic pigments are each time more focused on obtaining $CeO_2$ pigments in the form of fine nanosized particles with high surface area, because these features influence colour intensities [12,17,18]. Namely, the properties of the obtained pigments can be controlled by the incorporation of another element into the $CeO_2$ lattice using different processes of synthesis and modification [12,19–23]. The colouring mechanism is based on the charge transfer transition from $O_{2p}$ to $Ce_{4f}$ within the $CeO_2$ band structure, which can be modified by the introduction of an additional electronic level between the anionic $O_{2p}$ valence band and the cationic $Ce_{4f}$ conduction band [7]. The process of ceria ($CeO_2$) doping with different ions ($Ru^{3+/4+}$, $Yb^{3+}$, $Er^{3+}$, $Y^{3+}$, $Gd^{3+}$, $Sm^{3+}$, $Dy^{3+}$, $Nd^{3+}$, $Pr^{3+/4+}$) by using the self-propagating reaction at room temperature (SPRT method) has proven to be a very easy and unique way to obtain pigments with stable structure, morphology and optical properties [12,23–27]. The SPRT procedure, which is one of the most promising because of several advantages over conventional methods [12,23–27], is based on the self-propagating room temperature reaction between metal nitrates and sodium hydroxide, whereby the required equipment is extremely simple and inexpensive. The reaction is spontaneous, whereas the stoichiometry of the final product precisely matches the tailored composition.

Because of the above mentioned advantages, $CeO_2$ doped with $Er^{3+}$ and $Pr^{3+}$ ($Ce_{1-x}Er_xO_{2-\delta}$ and $Ce_{1-x}Pr_xO_{2-\delta}$; $x = 0.05$), as new potential environmentally friendly non-toxic ceramic pink and red pigments, were synthesized using the SPRT method [12,18,24,26]. The parameter $\delta$ denotes oxygen deficiency, i.e. departure from stoichiometry, both because of the introduction of dopant cations ($x$), and because of intrinsic non-stoichiometry. In our previous research [12], various shades of pink colour were obtained for $Er^{3+}$ doped $CeO_2$ ($Ce_{1-x}Er_xO_{2-\delta}$; $x = 0.05$–$0.20$) at room temperature (25 °C) and after thermal treatment at 600, 900 and 1200 °C for 4 h in an air.

In this work, structure, morphology and optical properties of $Ce_{1-x}Er_xO_{2-\delta}$ and $Ce_{1-x}Pr_xO_{2-\delta}$ ($x = 0.05$) at room temperature (25 °C), and after thermal treatment at 600, 900 and 1200 °C for 15 min in air, were compared. Thermal treatment lasted only for 15 min because the ceramic pigment ($Ce_{1-x}Pr_xO_{2-\delta}$; $x = 0.05$) very quickly reached different hues of red colour at 600, 900 and 1200 °C. In addition, praseodymium ($Pr^{3+}$) was selected as a very suitable candidate for obtaining ceramic pigments with a range of shades of red colour [18], because of its lower valence state, comparing with ceria, and good incorporation in its crystal lattice. Furthermore, $Pr^{3+}$ doped $CeO_2$ has still been unused up to now as a ceramic pigment for colouring of different oxides and glass for the application in industrial production [28,29]. Here presented research was focused on the development of a novel class of potential environmentally friendly non-toxic pigments based on $CeO_2$ with different shades of pink and red colour, aiming to expand the range of ceramic pigments application in the industry.

In this study, optical properties of solid solutions based on $CeO_2$, after very short thermal treatment in air, were investigated in order to replace toxic red pigments in a potential application in industrial production.

## II. Experimental section

### 2.1. Materials and methods

Starting reactants used in the experiments were cerium nitrate hexahydrate ($Ce(NO_3)_3 \cdot 6\,H_2O$; Aldrich, USA), erbium nitrate pentahydrate ($Er(NO_3)_3 \cdot 5\,H_2O$; Aldrich, USA), praseodymium nitrate hexahydrate ($Pr(NO_3)_3 \cdot 6\,H_2O$; John Mathey) and sodium hydroxide (NaOH, Vetprom-Chemicals). The desired compositions of the solid solutions were calculated from the ion-packing model equation [30]. The concentrations of the starting reactants were calculated in accordance with the chemical formula of the final products ($Ce_{0.95}Er_{0.05}O_{2-\delta}$ and $Ce_{0.95}Pr_{0.05}O_{2-\delta}$) [24,26], which were derived from the reactions (1) and (2):

$$(1-x)Ce(NO_3)_3 \cdot 6\,H_2O + xEr(NO_3)_3 \cdot 5\,H_2O + 3\,NaOH + (1/2-\delta)O_2 \longrightarrow Ce_{1-x}Er_xO_{2-\delta} + 3\,NaNO_3 + yH_2O \quad (1)$$

$$2\,(1-x)Ce(NO_3)_3 \cdot 6\,H_2O + xPr(NO_3)_3 \cdot 6\,H_2O + 6\,NaOH + (1/2-\delta)O_2 \longrightarrow 2\,Ce_{1-x}Pr_xO_{2-\delta} + 6\,NaNO_3 + 15\,H_2O \quad (2)$$

The starting chemicals were hand mixed [18,26] in alumina mortar for 15 min and then exposed to air for 3 h, which provided required energy for total termination of reaction according to the equation (1). For the removal of $NaNO_3$ the entire mixture was dispersed in water, and rinsing was performed in a Centurion 102 D centrifuge at 3000 rpm for 10 min. The procedure was performed three times with distilled water and twice with ethanol. The absence of $NaNO_3$ was confirmed by the titration analysis of the powder on Na using EDTA as the titrant. After drying at 100 °C for 24 h, the powders were thermally treated at 600, 900 and 1200 °C for 15 min in ambient atmosphere.

### 2.2. Characterization

All powders were characterized at room temperature by X-ray powder diffraction (XRPD) using an Ultima

IV Rigaku diffractometer, equipped with Cu $K_{\alpha 1,2}$ radiation, using a generator voltage of 40.0 kV and a generator current of 40.0 mA. The $2\theta$ range of 20–80° was used for all powders in a continuous scan mode with the scanning step size of 0.02° and the scan rate of 2 °/min. Phase analysis was performed using the PDXL2 software (version 2.0.3.0), with reference to the patterns of the International Centre for Diffraction Data database (ICDD), version 2012. XRPD method was also used to evaluate the crystallite size ($D_{XRPD}$) and lattice parameter ($a_{XRPD}$) as a function of temperature. Assuming that line broadening ($\beta = \beta' + \beta''$) is the sum of the contributions attributed to the crystalline size ($D_{XRPD}$) and microstrain ($e_{XRPD}$), which can be written as $\beta' = 1/(D_{XRPD} \cdot \cos\theta)$ and $\beta'' = 4e_{XRPD} \cdot \tan\theta$, the crystallite size and microstrain can be determined from the linear relationship between $\beta\cos\theta$ and $4\sin\theta$, where $\theta$ is the Bragg diffraction angle, and microstrain is $e_{XRPD} = \Delta d/d$ ($\Delta d$ is the displacement of the lattice) [31]. Before measurement, the angular correction was done using high quality Si standard. Lattice parameters were refined from the data using the least square procedure. Standard deviation was about 1%.

Raman spectra were collected in the spectral range from 300–700 $cm^{-1}$ using a DXR Raman microscope (Thermo Scientific, USA) equipped with a diode pumped solid state high-brightness laser (532 nm), an Olympus optical microscope and a CCD detector. Laser power was kept constant at 1 mW. The analysis of the scattered light was carried out using a spectrograph with grating of 900 lines/mm.

Transmission electron microscopy (TEM) analysis of investigated samples was carried by using JEOL JEM-2100 at 200 kV.

Microstructure and morphology of the investigated samples were observed using the field emission-scanning electron microscopy (FE-SEM) analysis (TESCAN Vega TS5130MM). The samples were precoated with a several-nanometre thick layer of gold before observation. A Fine Coat JFC-1100 ION SPUTTER Company JEOL device was used for the coating procedure.

Particle size distribution was determined from the obtained TEM and FE-SEM micrographs, immediately after they had been taken, using the Digital Micrograph software. Approximately 40 particles from each micrograph were chosen for the measurements. The diameter of the particles was measured manually, on screen and the result was recalculated into particle sizes using the Digital micrograph software. The mean value was taken as the relevant particle size of the powder.

The EDS analysis was carried out at the invasive electron energy of 30 keV by means of a QX 2000S device by Oxford Microanalysis Group. The maximum resolution was 0.4 nm.

Fourier transform infrared (FTIR) spectra of the samples were collected before and after the heat treatment at different temperatures by using a Perkin Elmer Spectrum Two FTIR spectrometer in the transmission mode. Pressed KBr pellets (technique 1 : 100) were recorded in the range from 450 to 4000 $cm^{-1}$ with the resolution of 4 $cm^{-1}$.

Optical properties were analysed by using a diffuse reflectance (DR) Thermo Electron Nicolet Evolution 500 spectrophotometer. Labsphere USRS-99-010 was used as the reflectance standard. The spectra were registered in the wavelength range from 350 to 800 nm and corresponding diffuse reflectance curves were recorded. Scan speed, step recording and bandwidth were 240 nm/min, 1 nm and 4 nm, respectively.

The analysis of colour characteristics of all samples was performed according to the CIE $L^*a^*b^*$ (1976) standard, using illuminant C spectral energy distribution. In this system, $L^*$ is the colour lightness ($L^* = 0$ for black and $L^* = 100$ for white), $a^*$ is the green (−)/red (+) axis, and $b^*$ is the blue (−)/yellow (+) axis, and their values were calculated according to the CIE $L^*a^*b^*$ standard.

## III. Results and discussion

The X-ray diffraction patterns of all obtained doped ceria powders ($Ce_{1-x}Er_xO_{2-\delta}$ and $Ce_{1-x}Pr_xO_{2-\delta}$; $x = 0.05$) are shown in Fig. 1. Regardless of the dopant type or

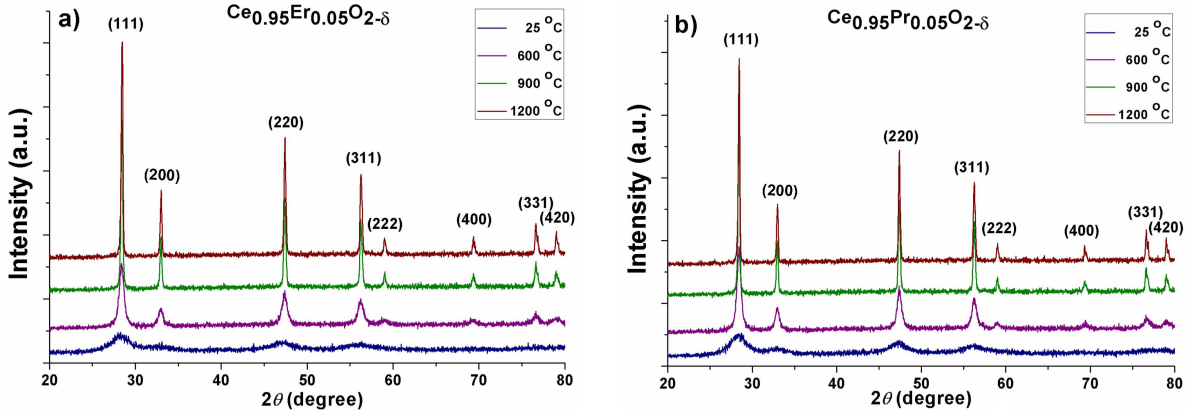


**Figure 1. XRPD patterns of: a) $Ce_{0.95}Er_{0.05}O_{2-\delta}$ and b) $Ce_{0.95}Pr_{0.05}O_{2-\delta}$ powders, thermally treated in air for 15 min at different temperatures**

**Table 1. Lattice parameters obtained by ion-packing model ($a_{ipm}$), lattice parameter ($a_{XRPD}$), crystallite size ($D_{XRPD}$) and microstrain ($e_{XRPD}$) obtained by XRPD analysis, and particle size obtained by TEM and FE-SEM of investigated samples at different temperatures**

| Sample | $a_{ipm,Er^{3+}}$ [Å] | $a_{ipm,Pr^{3+}}$ [Å] | $a_{ipm,Pr^{4+}}$ [Å] | $a_{XRPD}$ [Å] | $D_{XRPD}$ [nm] | $e_{XRPD}$ [%] | Particle size [nm] |
|---|---|---|---|---|---|---|---|
| 25 °C | | | | | | | |
| $Ce_{0.95}Er_{0.05}O_{2-\delta}$ [24] | 5.4091 | - | - | 5.4023 | 3.72 | 0.87 | 3.5* |
| $Ce_{0.95}Pr_{0.05}O_{2-\delta}$ | | 5.4231 | 5.4040 | 5.4410 | 2.39 | 1.07 | 2.3* |
| 600 °C | | | | | | | |
| $Ce_{0.95}Er_{0.05}O_{2-\delta}$ | 5.4091 | - | - | 5.3996 | 12.68 | 0.35 | 12.2* |
| $Ce_{0.95}Pr_{0.05}O_{2-\delta}$ | - | 5.4231 | 5.4040 | 5.4181 | 10.66 | 0.87 | 10.1* |
| 900 °C | | | | | | | |
| $Ce_{0.95}Er_{0.05}O_{2-\delta}$ | 5.4091 | - | - | 5.3895 | 32.23 | 0.11 | 32.0** |
| $Ce_{0.95}Pr_{0.05}O_{2-\delta}$ | | 5.4231 | 5.4040 | 5.4120 | 29.63 | 0.12 | 27.9** |
| 1200 °C | | | | | | | |
| $Ce_{0.95}Er_{0.05}O_{2-\delta}$ | 5.4091 | | | 5.3854 | 36.81 | 0.08 | 37.9** |
| $Ce_{0.95}Pr_{0.05}O_{2-\delta}$ | | 5.4231 | 5.4040 | 5.4103 | 35.06 | 0.07 | 34.5** |

* TEM, ** FE-SEM

heat treatment temperature, all obtained solid solutions exhibited the single-phase fluorite crystal structure with $Fm3m$ space group [18]. High solubility of the dopants in the obtained solid solutions and retaining of the fluorite crystalline structure can be attributed to their nanometric dimensions. The structure information was taken from the American Mineralogist Crystal Data Structure Base (AMCDSB). The reflections for the as-prepared powders, that had not been thermally treated, were significantly broadened (Fig. 1), indicating small crystallite size ($D_{XRPD}$) and/or microstrain ($e_{XRPD}$) (Table 1). Because of very low crystallinity, the XRPD patterns exhibited very diffuse diffraction lines, in such a way that some XRD peaks are not visible (i.e. 222, 400, 331, 420). However, after the thermal treatment, the powders were depicted by XRPD diagrams with sharper diffraction lines, which is in line with the increase of crystallite sizes $D_{XRPD}$ (Table 1).

The results of lattice parameters ($a_{XRPD}$), crystallite size ($D_{XRPD}$) and microstrain ($e_{XRPD}$) of the $Ce_{0.95}Pr_{0.05}O_{2-\delta}$ and $Ce_{0.95}Er_{0.05}O_{2-\delta}$ powders are shown in Table 1. It was found that the crystallite size of the doped ceria powders increases with the increase of temperature from 25–1200 °C. This is in a good agreement with the lattice parameter values, which decreased with increasing thermal treatment temperature decreased, and approached the value of the standard pure ceria crystal lattice [23], as well as the theoretical values obtained by ion-packing model ($a_{ipm}$) (Table 1). Namely, according to Shannon's compilation [32], the ionic radii of $Ce^{4+}$, $Ce^{3+}$, $Er^{3+}$, $Pr^{3+}$ and $Pr^{4+}$ are 0.970, 1.143, 1.004, 1.126 and 0.960 Å, respectively, for eightfold coordination. Additionally, it is known that $CeO_2$ crystal lattice contains $Ce^{4+}$ and $Ce^{3+}$ ions per core-shell model [33, 34]. It was found that most of $Ce^{3+}$ is located at the surface [33,34]. All above mentioned indicates that doping process can lead to the substitution of $Ce^{4+}$ and $Ce^{3+}$ ions with $Er^{3+}$ and $Pr^{3+}$ ions (confirmed by Raman spectroscopy results presented further in the text). Besides, it is also known that praseodymium ions can easily change the oxidation state ($Pr^{3+} \leftrightarrow Pr^{4+}$) [35,36]. Since the ionic radius of $Er^{3+}$ is smaller than the ionic radius of $Ce^{3+}$ and larger than the ionic radius of $Ce^{4+}$, the doping process can lead to the dilation of the lattice and the reduction of the lattice parameter values in comparison with the pure $CeO_2$ [23]. With increasing temperature, the lattice parameter value of the $CeO_2$ doped with $Er^{3+}$ ions further decreased. Such behaviour can be explained by the loss of oxygen vacancies because of the influence of high temperature. Namely, theoretical calculations predict that oxygen vacancies tend to migrate from the nanoparticle's interior to the surface [24,37]. According to our results it seems that the migration of oxygen vacancies was intensified when the samples were exposed to higher temperatures. In the case of $Er^{3+}$ doped ceria subjected to the high temperature heat treatment (900 and 1200 °C), oxygen vacancies probably migrated from $CeO_2$ nanoparticles' interior to the surface, and furthermore, left the sample surface thus leading to lattice stabilization. This assumption can be supported by the obtained Raman spectra (Fig. 2a), where the Raman intensity of "vacancies mode" decreased as the consequence of the heat treatment. On the other hand, the lattice of the ceria doped with praseodymium ions exhibited expansion, which can be explained in terms of higher oxygen vacancy concentration because of possible presence of $Ce^{3+}$, $Pr^{3+}$ and $Pr^{4+}$ ions. Besides, the lattice parameter of the $CeO_2$ doped with $Pr^{3+/4+}$ ions gradually decreased with increasing temperature, although Raman spectroscopy confirmed increased Raman intensity of "vacancies mode". The reason for this behaviour would have to be the change of the oxidation state of $Pr^{3+}$ in $Pr^{4+}$ (0.960 Å), with similar ionic radius as $Ce^{4+}$ ion (0.970 Å), which explains the decrease in lattice parameter with the formation of a new oxygen vacancy (confirmed by Raman spectroscopy; Fig. 2b). Additionally, all treated samples exhibited strong influence of temperature on the microstrain, where with in-

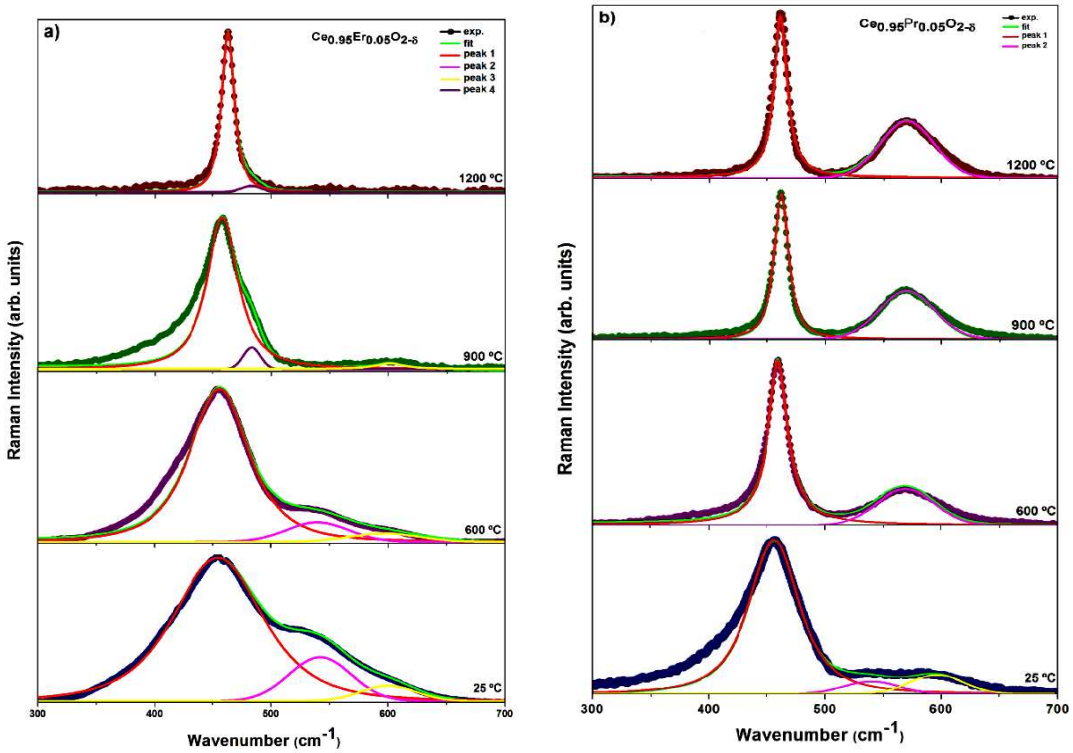


**Figure 2. De-convoluted Raman spectra of: a) $Ce_{0.95}Er_{0.05}O_{2-\delta}$ and b) $Ce_{0.95}Pr_{0.05}O_{2-\delta}$ at different temperatures**

creased temperature the values of the crystallite sizes increases together with lowering the microstrain (Table 1). According to our findings, the decrease of microstrain can lead to lattice stabilization, which was achieved by two completely different processes. Thus, in the case of the samples containing $Er^{3+}$ that lacks in the oxidized form of erbium ($Er^{4+}$) lattice stabilization (reflected in decreasing microstrain and lattice parameter) was achieved by oxygen vacancies leaving the sample surface. On the other hand, with the samples containing praseodymium ions, the change in the oxidation state (from $Pr^{3+}$ to $Pr^{4+}$) that has similar ionic radius and the same oxidation state as $Ce^{4+}$ ions, leads to the decreased microstrain and lattice parameter values and general lattice stabilization.

The identification of the Raman spectrum of the materials based on $CeO_2$ allowed the information about their potential behaviour and applications. Especially, based on Raman signature for oxygen vacancies in the above mentioned materials, the mechanism of their behaviour under the influence of temperature can be defined. The Raman spectra of the as-prepared $Ce_{0.95}Er_{0.05}O_{2-\delta}$ and $Ce_{0.95}Pr_{0.05}O_{2-\delta}$ powders (25 °C) and those thermally treated in air for 15 min at different temperatures (600, 900 and 1200 °C) are presented in Fig. 2. It is well documented that the main feature in the Raman spectrum of the pure and stoichiometric $CeO_2$ with fluorite structure is a single allowed Raman mode of the first order ($F_{2g}$ symmetry), positioned at the wavenumber of 465 cm$^{-1}$ [23]. This mode occurs as a result of the symmetric breathing mode of O atoms around each cation ($CeO_8$, the lattice vibration). In the present work, the obtained nanopowders at room temperature (25 °C; Fig. 2) exhibited shifting of this mode to lower energies (457 and 450 cm$^{-1}$) with increased line width and expressed asymmetry at the lower energy side. These changes in Raman peak profile [18,23] may be due to the nanosized effects such as phonon confinement, inhomogeneous strain and non-stoichiometry. After thermal treatment in air during 15 min at different temperatures (600, 900 and 1200 °C), the Raman mode was shifted to higher frequencies both for $Ce_{0.95}Er_{0.05}O_{2-\delta}$ (460, 462 and 463 cm$^{-1}$, respectively), and for the $Ce_{0.95}Pr_{0.05}O_{2-\delta}$ (456, 459 and 463 cm$^{-1}$, respectively), with the reduction of line width (Table 2) and the appearance of symmetry. All these characteristics of the Raman peak profile showed that thermal treatment led to grain growth and the formation of better ordered structures, which was confirmed by XRPD (Fig. 1; Table 1), TEM (Figs. 3a and 3b) and FE-SEM analyses (Figs. 3c and 3d).

In addition to the mentioned Raman mode of the first order, the Raman spectra of the powders based on $CeO_2$ showed the presence of additional second order modes positioned at about 550 and 600 cm$^{-1}$ [12,23], and defined as Raman signature for oxygen vacancies. The modes positioned at about 550 and 600 cm$^{-1}$ are assigned to intrinsic and extrinsic oxygen vacancies, generated in $CeO_2$ lattice with reduction in particle size and doping process, respectively [12,23]. Namely, with particle size decreasing the overall free surface of the powder increases, enabling easier release of oxygen from

the lattice, thus leaving a vacancy and two electrons localized on a cerium atom. This process causes the formation of $Ce^{3+}$ ions (lowering of $Ce^{4+}$ valence, which is due to electroneutrality demands) and the emergence of the Raman mode at around 600 $cm^{-1}$ (Fig. 2) [23]. On the other hand, for the doped nanopowders additional Raman mode at around 550 $cm^{-1}$ was attributed to oxygen vacancies introduced into the ceria lattice when $Ce^{4+}$ ions were replaced with cations of lower valence state [12,23] (in this case oxidation numbers were 3+). At 25 °C the occurrence of the mode originating from the oxygen vacancies can be explained by the substitution of two $Ce^{4+}$ ions with two dopant ions ($Er^{3+}$ or $Pr^{3+}$), when one oxygen vacancy is introduced into the ceria lattice in order to maintain the electrical neutrality [24,26]. However, with increasing heat treatment temperature, the mentioned mode for the $Ce_{0.95}Er_{0.05}O_{2-\delta}$ was slowly disappearing [12], while for the $Ce_{0.95}Pr_{0.05}O_{2-\delta}$ these modes merged into one at about 570 $cm^{-1}$, whose intensity increased with increasing temperature [18,24]. This behaviour of the mode originating from the oxygen vacancies introduced into the ceria lattice can be explained by two different mechanisms for the two dopants:

1. With increasing temperature, the Raman intensity of "vacancies mode" related to the $Er^{3+}$ doped $CeO_2$ decreases (Fig. 2a), which can be due to the intensified migration of oxygen vacancies towards the surface of the sample and their loss under the influence of temperature. The loss of oxygen vacancies due to the influence of temperature was in agreement with theoretical calculations which also predict their migration from the nanoparticles' interior to the surface [24,37]. Thus, under the influence of increased temperature, the migration of oxygen vacancies was intensified, followed by their leaving of the sample surface at higher temperatures. The higher temperature, the more eased leaving of sample surface was. This mechanism was supported by the recorded Raman spectra (Figs. 2a and 3), where it is clear that Raman intensity of "vacancies mode" decreases with increasing temperature of the heat treatment.
2. With increasing temperature, the Raman "vacancies modes" related to the praseodymium doped $CeO_2$ appeared originating from the presence of $Ce^{3+}$ ions. They underwent merging in one mode at about 570 $cm^{-1}$, whose intensity increased with increasing temperature (Fig. 2b). This can be due to the presence of $Ce^{3+}$ and $Pr^{3+}$, but also $Pr^{4+}$ ions (0.960 Å) in $CeO_2$ structure, whose ionic radii are similar to that of $Ce^{4+}$. Namely, the praseodymium ions can easily change the oxidation state ($Pr^{3+} \leftrightarrow Pr^{4+}$) [24,36], which allows the stabilization of the crystal lattice, formation of a new oxygen vacancy and increase of the Raman intensity of "vacancies mode" (Figs. 2b and 3).

Thus, according to the literature [18,23,24] and here presented results (Figs. 2 and 3), the intensity of peaks at 550 and 600 $cm^{-1}$ is dependent on the number of vacancies. Their absence or presence may indicate the mechanisms of vacancy behaviour with increasing tempera-

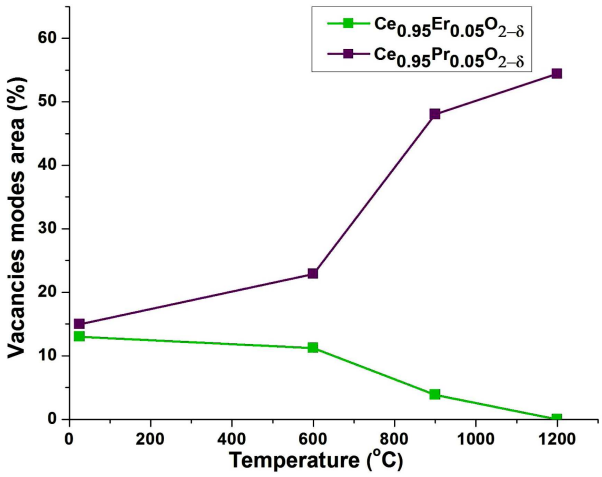


**Figure 3. Vacancies modes area as a result of Raman peak's area sum at 550 and 600 $cm^{-1}$ illustrating two different mechanisms of vacancy behaviour with increasing temperatures**

**Table 2. Results of the de-convolution of Raman spectra of the $Ce_{0.95}Er_{0.05}O_{2-\delta}$ and $Ce_{0.95}Pr_{0.05}O_{2-\delta}$ powders, at room temperature (25 °C) and those thermally treated at different temperatures (600, 900 and 1200 °C), in air for 15 min**

| Sample | Area [%] | | | | |
|---|---|---|---|---|---|
| | Peak 1 (465 $cm^{-1}$) | FWHM (465 $cm^{-1}$) | Peak 2 (550 $cm^{-1}$) | Peak 3 (600 $cm^{-1}$) | Peak 4 (480 $cm^{-1}$) |
| 25 °C | | | | | |
| $Ce_{0.95}Er_{0.05}O_{2-\delta}$ | 86.95 | 60.05 | 7.47 | 5.57 | - |
| $Ce_{0.95}Pr_{0.05}O_{2-\delta}$ | 85.03 | 42.14 | 5.87 | 9.10 | - |
| 600 °C | | | | | |
| $Ce_{0.95}Er_{0.05}O_{2-\delta}$ | 88.74 | 53.21 | 6.59 | 4.67 | - |
| $Ce_{0.95}Pr_{0.05}O_{2-\delta}$ | 77.10 | 15.77 | 22.90 | | - |
| 900 °C | | | | | |
| $Ce_{0.95}Er_{0.05}O_{2-\delta}$ | 90.82 | 31.98 | - | 3.87 | 5.31 |
| $Ce_{0.95}Pr_{0.05}O_{2-\delta}$ | 51.96 | 11.87 | 48.04 | | - |
| 1200 °C | | | | | |
| $Ce_{0.95}Er_{0.05}O_{2-\delta}$ | 95.36 | 12.88 | - | - | 4.64 |
| $Ce_{0.95}Pr_{0.05}O_{2-\delta}$ | 45.58 | 11.85 | 54.42 | | - |

tures, and improvement of properties for potential applications [12,25–27]. It is evident from Fig. 3 that the total vacancies content for the $Er_3^+$ doped $CeO_2$ decreased, while it increased in the case of $Pr^{3+/4+}$ doped $CeO_2$.

Additional mode positioned at about 480 $cm^{-1}$, which occurs in the case of the $Ce_{0.95}Er_{0.05}O_{2-\delta}$ thermally treated at the temperature at 900 °C and above, can be a result of the surface mode appearing in the case of very small crystallites like $CeO_{2-x}$ [37]. The appearance of this infrared active mode in the Raman spectra can be explained by the lack of long-range order in small crystallites and by the relaxation of the selection rules as a consequence of the defective structure. With further increase of temperature, the intensity of the mentioned mode decreases (Fig. 2a), which confirmed the formation of ordered $CeO_2$ structures. The occurrence of this mode is in correlation with the FTIR results, and according to our knowledge, its presence in both Raman and FTIR spectra of the doped $CeO_2$ nanocrystals is first reported here (discussed below).

The TEM images of the as-prepared $Ce_{0.95}Er_{0.05}O_{2-\delta}$ and $Ce_{0.95}Pr_{0.05}O_{2-\delta}$ nanopowders at 25 °C and those thermally treated at 600 °C for 15 min in air, are presented in Figs. 4a and 4b. In all the images the presence of the agglomerates and formed aggregates can be seen, which results from the natural tendency of crystallites to agglomerate [12,23,26]. The first reason for this is energetically more stable configuration of the agglomerated form, while the second reason is the possibility of the crystallite growth. The additional information on the morphology and microstructure of the $Ce_{0.95}Er_{0.05}O_{2-\delta}$ and $Ce_{0.95}Pr_{0.05}O_{2-\delta}$ nanopowders thermally treated at 900 and 1200 °C for 15 min in air were obtained by using FE-SEM technique (Figs. 5a and 5b). These two powders show homogeneous structure and grain growth upon thermal treatment can be traced, indicating good thermodynamical stability. It is noteworthy that the mean particle size calculated from TEM (Fig. 4) and FE-SEM images (Fig. 5) shows increase with increasing heat treatment temperature for both doped $CeO_2$ powders (Table 1). The results obtained from the TEM images indicate that the mean particle size was below 4 nm and that it differed at most by 1 nm from those obtained by XRPD. Besides, the results indicate that the average grain size measured from the FE-SEM images was smaller than 40 nm and it differed at most by 2 nm from those obtained by XRPD. This confirms the consistence of the TEM and FE-SEM results with the results obtained by XRPD.

Corresponding EDS spectra of the $Ce_{0.95}Er_{0.05}O_{2-\delta}$ and $Ce_{0.95}Pr_{0.05}O_{2-\delta}$ nanopowders thermally treated at 1200 °C in air for 15 min (Fig. 6), and mean values of the $Ce^{3+/4+}/Er^{3+}$ and $Ce^{3+/4+}/Pr^{3+/4+}$ chemical ratios confirmed that $Er^{3+}$ and $Pr^{3+/4+}$ ions in the concentrations of 5% ($Ce^{3+/4+}/Er^{3+}$ = 95.23/4.77, $Ce^{3+/4+}/Pr^{3+/4+}$ = 95.11/4.89) are successfully incorporated into the host matrix.

In Fig. 7, FTIR spectra of the as-prepared $Ce_{0.95}Er_{0.05}O_{2-\delta}$ and $Ce_{0.95}Pr_{0.05}O_{2-\delta}$ powders (25 °C) and those thermally treated at different temperatures (600, 900 and 1200 °C) in air for 15 min are presented. Both spectra show a large absorption band located at around 480 $cm^{-1}$. This band can be attributed to the Ce–O stretching vibration [12,38,39] and corresponds to the $F_{1u}$ IR active mode of the $CeO_2$ fluorite structure. Additionally, the mode positioned at about

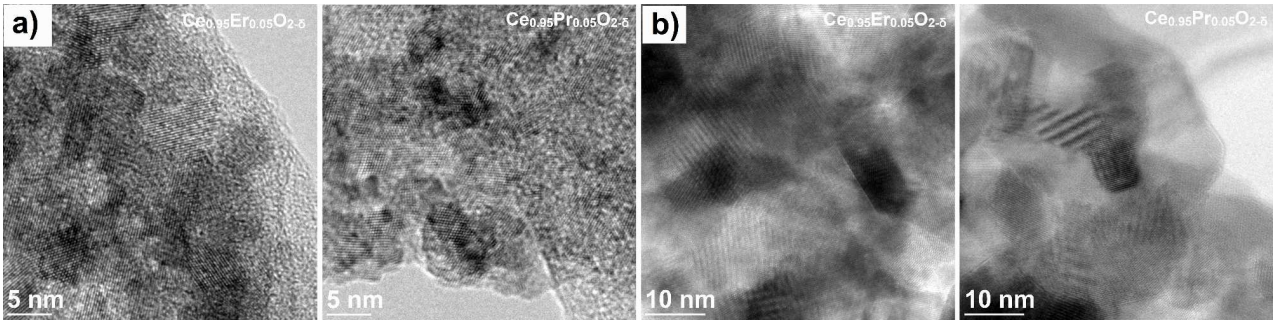


**Figure 4. TEM images of investigated samples: a) as-prepared and b) thermally treated at 600 °C**

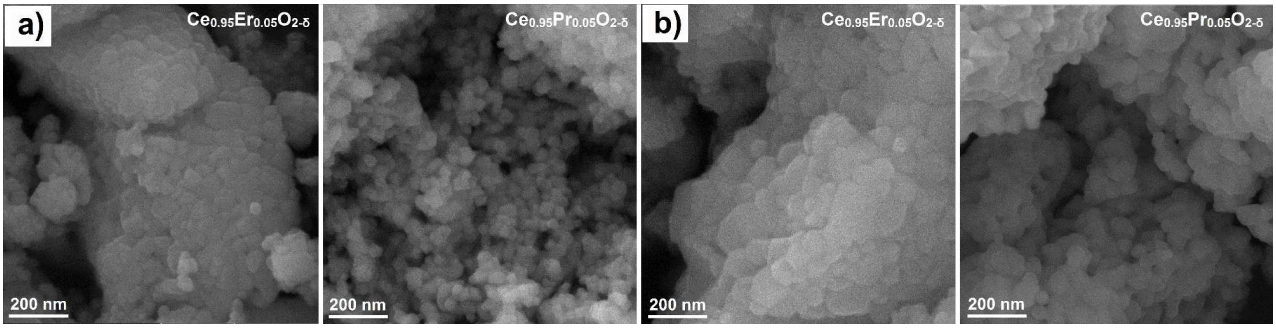


**Figure 5. FE-SEM images of investigated samples thermally treated at: a) 900 and b) 1200 °C**

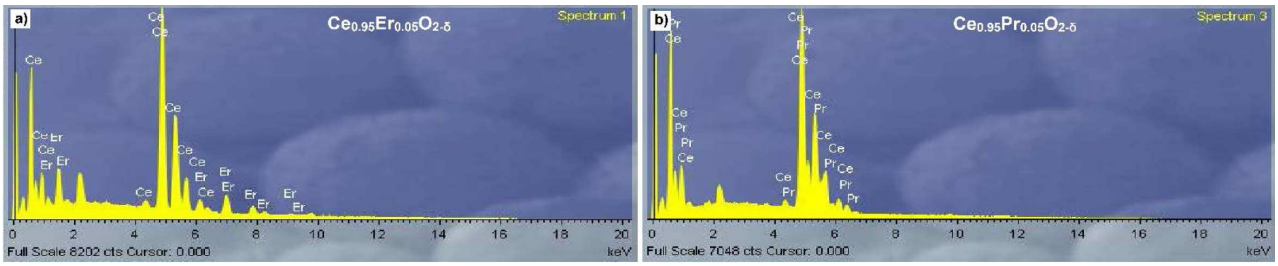


**Figure 6. EDS spectra of: a) $Ce_{0.95}Er_{0.05}O_{2-\delta}$ and b) $Ce_{0.95}Pr_{0.05}O_{2-\delta}$ samples thermally treated at 1200 °C**

480 $cm^{-1}$ was observed in Raman spectrum of the sample $Ce_{0.95}Er_{0.05}O_{2-\delta}$ and can be ascribed to a surface mode appearing in very small crystallites such as $CeO_{2-x}$ whose energy lies between the infrared active TO and LO phonons of $CeO_2$ [37]. As already mentioned, the appearance of this IR active mode in the Raman spectra can be explained by the lack of long-range order in small crystallites and by the relaxation of the selection rules as a consequence of defective structure. Furthermore, the bands located at around 720, 840, and 1060 $cm^{-1}$ can be attributed to the $CO_2$ asymmetric stretching vibration, $CO_3^{2-}$ bending vibration, and C–O stretching vibration, respectively [40]. These bands arise as the consequence of the reaction of atmospheric $CO_2$ with water and sodium hydroxide during the synthesis process, which leads to the adsorption of atmospheric $CO_2$ on the cations [21] and formation of "carbonate-like" species on the particle surfaces [38]. The bands at around 1360 and 1520 $cm^{-1}$ can be attributed to the vibrations of carbonate species [38,40]. The attenuation of the bands after heat treatment indicates that the carbonate species were thermally decomposed. The band located at around 1640 $cm^{-1}$ is attributed to the H–O–H bending vibration [21] and indicates the presence of water. Both groups' spectra contain a large band with the maximum located at around 3400 $cm^{-1}$, which can be attributed to the O–H stretching vibration [12]. It confirms the presence of moisture and structural water in the sample before its exposure to heat treatment. Since the band is attenuated in the spectrum collected after heat treatment at 1200 °C during 15 min in air, it can be concluded that some moisture was absorbed after calcination.

The temperature influence on the optical properties of the $Ce_{0.95}Er_{0.05}O_{2-\delta}$ and $Ce_{0.95}Pr_{0.05}O_{2-\delta}$, particularly the reflectance and band gap energy, was examined using DR UV-VIS spectrometry. Both samples have showed absorption maximum (complementary reflectance minimum) at around 380 nm, which is attributed to the charge transfer of $O_{2p} \rightarrow Ce_{4f}$ [41]. The reflectance curves for $Ce_{0.95}Pr_{0.05}O_{2-\delta}$ samples showed slow growth with increasing wavelength, reaching reflectance maximum at around 650 nm (red region). On the other hand, the reflectance curves for the $Ce_{0.95}Er_{0.05}O_{2-\delta}$ samples showed a sudden increase in reflectance with increasing wavelength and plateau was reached at around 450 nm (blue region). In addition, the diffuse reflectance spectra of the $Ce_{0.95}Er_{0.05}O_{2-\delta}$ and $Ce_{0.95}Pr_{0.05}O_{2-\delta}$ showed the absorption difference between the as-prepared (25 °C) and thermally treated (600, 900 and 1200 °C) samples (Fig. 8), respectively. For the $Ce_{0.95}Er_{0.05}O_{2-\delta}$ and $Ce_{0.95}Pr_{0.05}O_{2-\delta}$ samples that were not thermally treated, intensive reflectance occurred along the full range of electromagnetic spectrum. It is evident from Fig. 8 that increasing heat treatment temperature resulted in increasing absorption (decreasing of reflectance plateau), especially for the samples treated at 1200 °C. The intensive absorption peaks at 490, 520, 546, 652 and 677 nm were found on $Ce_{0.95}Er_{0.05}O_{2-\delta}$ reflectance plateau. Due to the increasing absorption at these wavelengths with increasing $Er^{3+}$ content in ceria lattice, these peaks are assigned to erbium ion transitions [12]. Since dopant $Er^{3+}$ ions replace $Ce^{4+}$ ions, they appear as new light absorbing species. The corresponding absorption bands and transition energies are presented in Fig. 9. According to our findings, the absorption peaks at 490,

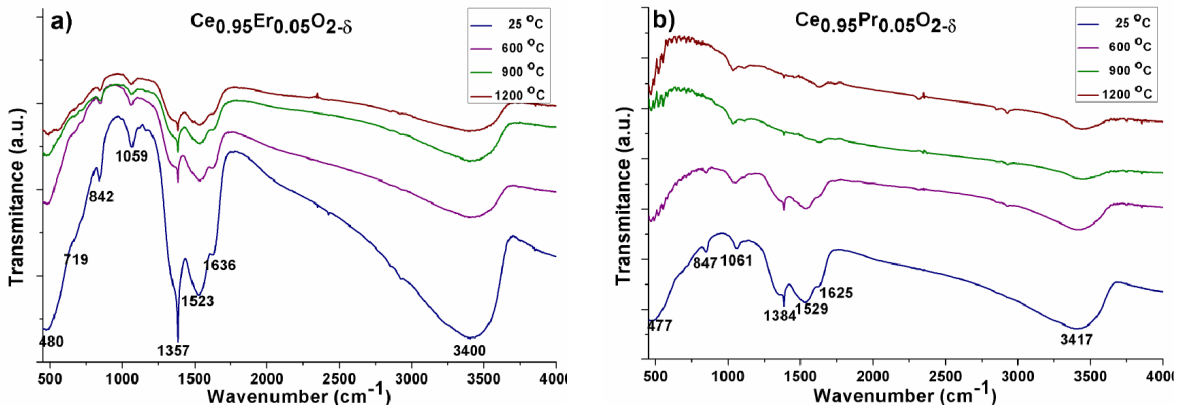


**Figure 7. FTIR spectra of: a) $Ce_{0.95}Er_{0.05}O_{2-\delta}$ and b) $Ce_{0.95}Pr_{0.05}O_{2-\delta}$ powders, thermally treated at different temperatures**

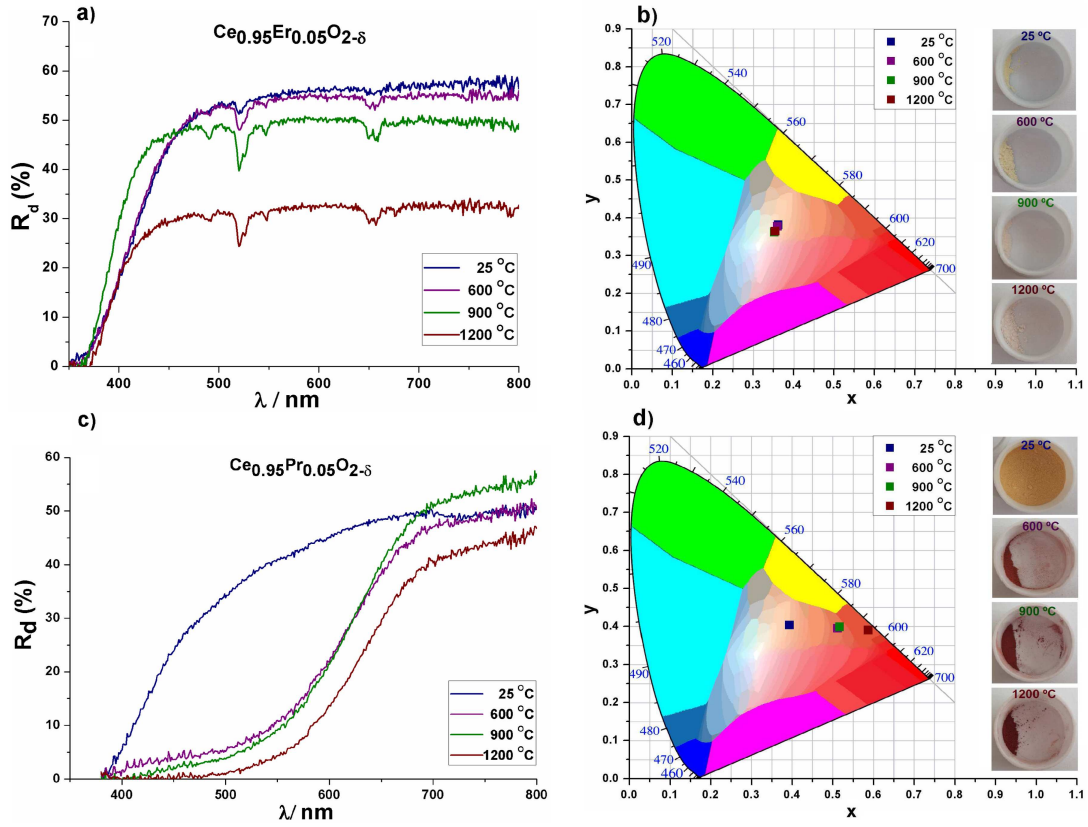


**Figure 8. The DR UV-VIS spectra (a and c) and chromatic diagram (b and d) of the $Ce_{0.95}Er_{0.05}O_{2-\delta}$ and $Ce_{0.95}Pr_{0.05}O_{2-\delta}$ powders, thermally treated at different temperatures in air for 15 min**

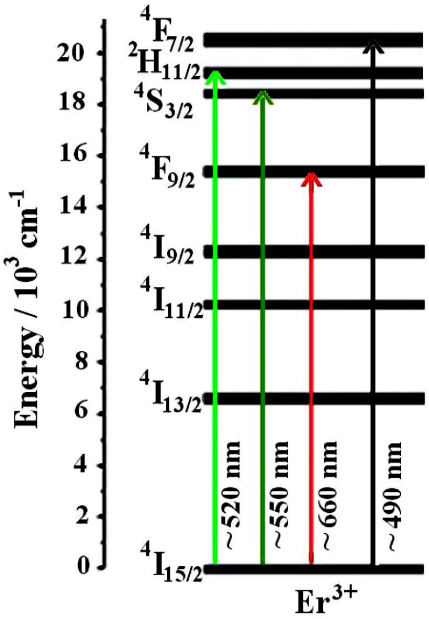


**Figure 9. Scheme of the energy levels and energy transitions of $Ce_{0.95}Er_{0.05}O_{2-\delta}$**

520, 550 and 660 nm are assigned to following energy transitions $^4I_{15/2}\rightarrow{}^4F_{7/2}$, $^4I_{15/2}\rightarrow{}^2H_{11/2}$, $^4I_{15/2}\rightarrow{}^4S_{3/2}$ and $^4I_{15/2}\rightarrow{}^4F_{9/2}$ [15,41].

Beside differences in the reflectance plateau $R$ [%], the temperature influence on the visible light absorption is evidenced as the shift of the reflectance curves towards larger wavelengths and it had much greater impact on the $Ce_{0.95}Pr_{0.05}O_{2-\delta}$ samples. The low energy shift signifies partial reduction of cerium to its trivalent state [42,43]. The reduction process ($Ce^{4+}\rightarrow Ce^{3+}$) for the applied experimental conditions occurred in the praseodymium doped $CeO_2$ samples rather than with erbium ions. This finding indicates that the $Ce^{4+}\rightarrow Ce^{3+}$ reduction process has important role in the lattice stabilization. Additionally, the band gap energies ($E_g$) of the $Ce_{0.95}Er_{0.05}O_{2-\delta}$ and $Ce_{0.95}Pr_{0.05}O_{2-\delta}$ samples treated at different temperatures 25, 600, 900 and 1200 °C were found (Table 3.). The band gap energy calculations were performed on the basis of the Tauc plot [44], and the Kubelka-Munk function [45]. The $E_g$ values were determined by the extrapolation of the linear part of the $[F(R) \times E]^2$ versus energy $E$ curves, where $F(R)$ is Kubelka-Munk function $F(R) = (1 - R)^2/(2R)$, and $R$ is reflectance.

Band gap width decreased with increasing heat treatment temperatures for both $Ce_{0.95}Er_{0.05}O_{2-\delta}$ and $Ce_{0.95}Pr_{0.05}O_{2-\delta}$ samples (Table 3). The greatest band gap values are determined for the $Ce_{0.95}Er_{0.05}O_{2-\delta}$ (3.25 eV) and $Ce_{0.95}Pr_{0.05}O_{2-\delta}$ (3.05 eV) samples that were not thermally treated. Because of slightly smaller band gap energy value for the praseodymium than for the as-prepared erbium doped sample (25 °C), it can be concluded that $Pr^{3+/4+}$ ion incorporation in $CeO_2$ enhanced lattice stabilization to a greater extent, comparing to $Er^{3+}$ ion. The samples treated at 600 °C exhibited

**Table 3. Calculated band gap energy, $E_g$ [eV], and colour coordinates ($L^*a^*b^*$) for the $Ce_{0.95}Er_{0.05}O_{2-\delta}$ and $Ce_{0.95}Pr_{0.05}O_{2-\delta}$ powders, thermally treated at different temperatures, in air for 15 min**

| Sample | Band gap $E_g$ [eV] | Colour measurement | | |
|---|---|---|---|---|
| | | $L^*$ | $a^*$ | $b^*$ |
| 25 °C | | | | |
| $Ce_{0.95}Er_{0.05}O_{2-\delta}$ [15] | 3.25 | 78.880 | -1.560 | 10.683 |
| $Ce_{0.95}Pr_{0.05}O_{2-\delta}$ | 3.05 | 70.351 | 1.548 | 22.616 |
| 600 °C | | | | |
| $Ce_{0.95}Er_{0.05}O_{2-\delta}$ | 3.22 | 78.144 | -1.268 | 9.103 |
| $Ce_{0.95}Pr_{0.05}O_{2-\delta}$ | 2.30 | 45.031 | 27.288 | 35.832 |
| 900 °C | | | | |
| $Ce_{0.95}Er_{0.05}O_{2-\delta}$ | 3.20 | 75.127 | 1.572 | 2.319 |
| $Ce_{0.95}Pr_{0.05}O_{2-\delta}$ | 2.27 | 43.491 | 30.892 | 44.19 |
| 1200 °C | | | | |
| $Ce_{0.95}Er_{0.05}O_{2-\delta}$ | 3.17 | 62.663 | 1.281 | 2.944 |
| $Ce_{0.95}Pr_{0.05}O_{2-\delta}$ | 2.13 | 33.633 | 34.299 | 49.291 |

greater band gap reduction (the greatest band gap energy drop) in comparison with the as-prepared samples. Low energy shift of the $Er^{3+}$ doped samples insignificantly varies with the increase of heat treatment temperatures. The observed energy drop was significant for the $Ce_{0.95}Pr_{0.05}O_{2-\delta}$ samples. It is related to oxygen vacancies (detected with Raman spectroscopy, Table 2), as well as the $Ce^{4+}\rightarrow Ce^{3+}$ reduction process. The latter results in the increase of $Ce^{3+}$ concentration that can cause energy shift to a lower level [43].

Regarding the colour of samples, it is well-known that the colour of absorbed light includes the band gap energy, but also all colours of higher energy (shorter wavelength), because electrons can be excited from the valence band to a range of energies in the conduction band. Thus, we can easily calculate absorbed light ($\lambda < 1240.8/E_g$) using $E_g = hc/\lambda$, where $h$ is Planck's constant and $c$ is the speed of light in vacuum. Therefore, wide band gaps obtained for $Ce_{0.95}Er_{0.05}O_{2-\delta}$ at different temperatures (from 25 to 1200 °C) correspond to 382, 385, 388 and 391 nm, respectively and thus shades from yellow toward light pink appeared. Otherwise, band gaps obtained for $Ce_{0.95}Pr_{0.05}O_{2-\delta}$ at different temperatures (from 25 to 1200 °C) correspond to 407, 539.5, 547 and 583 nm, respectively. The $Ce_{0.95}Pr_{0.05}O_{2-\delta}$ at 25 °C has a band gap of 3.05 eV and thus absorbs light with $\lambda < 407$ nm and appears yellow, while $Ce_{0.95}Pr_{0.05}O_{2-\delta}$ at 600 and 900 °C with $\lambda < 539.5$ nm, $\lambda < 547$ nm appear reddish-orange (the colours of light reflected) because it absorbs green, blue and violet light. The $Ce_{0.95}Pr_{0.05}O_{2-\delta}$ at 1200 °C absorbs light with $\lambda < 583$ nm and appears a darker shade of reddish-orange because it besides green, blue and violet light absorbs and yellow light. Additionally, it can be concluded that abundance of defects related to oxygen vacancies as well as the $Ce^{4+}\rightarrow Ce^{3+}$ reduction process, resulted in the narrowed band gap and enhanced optical absorption in $Ce_{0.95}Pr_{0.05}O_{2-\delta}$ at elevated temperatures.

Based on certain changes of band gap width and colour characteristics of the $Ce_{0.95}Er_{0.05}O_{2-\delta}$ and $Ce_{0.95}Pr_{0.05}O_{2-\delta}$ samples (Figs. 8a and 8c), the values of chromatic coordinates for both groups of compounds at room temperature (25 °C), and heat treated at 600, 900 and 1200 °C for 15 min in air are illustrated in chromatic diagrams (Figs. 8b and 8d). The calculated values of the band gap for both $Ce_{0.95}Er_{0.05}O_{2-\delta}$ and $Ce_{0.95}Pr_{0.05}O_{2-\delta}$ samples are presented in Table 3. From the corresponding $L^*a^*b^*$ coordinates (Table 3), it is obvious that colour changes are very intensive for the heat treated $Ce_{0.95}Pr_{0.05}O_{2-\delta}$ sample. On the other hand, changes of the colour characteristics of the $Ce_{0.95}Er_{0.05}O_{2-\delta}$ are somewhat lower in intensity (Table 3). At the same time, increasing contribution of the coordinates $a^*$ and $b^*$ was in compliance with the progressive decrease of luminosity ($L^*$), especially for the $Ce_{0.95}Pr_{0.05}O_{2-\delta}$ sample (from 70.351 to 33.633). Therefore, the colour shifted with increasing temperature from yellow toward light pink hue (increasing $a^*$) and became more saturated (decreasing $L^*$) for the $Ce_{0.95}Er_{0.05}O_{2-\delta}$ sample. For the $Ce_{0.95}Pr_{0.05}O_{2-\delta}$ sample the colour shifted from yellow to dark-red hue. Successful incorporation of $Er^{3+}$ as well as $Pr^{3+/4+}$ ions in the lattice of $CeO_2$ is thus confirmed. The most pink and red hues (the highest values of coordinates $a^*$) are achieved for the pigments thermally treated at the highest temperature (1200 °C). Thus, according to Figs. 8b and 8d, and their corresponding insets (visual appearance), the colour and intensity of the pigments was dependent on the composition (dopant ion type) and heat treatment temperature, and the colour of the pigments could vary from white-pink to dark-red hue.

## IV. Conclusions

Nanostructured non-toxic $Ce_{0.95}Er_{0.05}O_{2-\delta}$ and $Ce_{0.95}Pr_{0.05}O_{2-\delta}$ oxides, as pink and red colour compounds, were successfully synthesized by low cost self-propagating room temperature method. All cerium oxide powders before (at 25 °C) and after heat treatment (treated at 600, 900 and 1200 °C during 15 min in air) had crystal structure of the fluorite type with $Fm3m$ space group, which confirmed the structural

and thermal stability of the obtained solid solutions. Particle sizes remained within the nanometric range along with temperature increase from 25–1200 °C for all obtained pigments. The absence of oxygen vacancies in the structure of the obtained pigments, examined by Raman spectroscopy, may indicate their future potential applications. Furthermore, the colour changes depended on the composition (dopant ion type) and the heat treatment temperature. Increased temperature resulted in colour variation from yellow to light-pink hue for $Ce_{0.95}Er_{0.05}O_{2-\delta}$, and from yellow to dark-red hue for $Ce_{0.95}Pr_{0.05}O_{2-\delta}$. Another consequence of the increase of heat treatment temperature was the increase of crystallite size and light absorption, where the edge of absorption of visible light shifted toward lower energies.

The structure, morphology and optical properties of nanometric $Ce_{0.95}Er_{0.05}O_{2-\delta}$ and $Ce_{0.95}Pr_{0.05}O_{2-\delta}$ synthesized in this work, suggest that these compounds may be interesting to be used as pigments for a wide area of applications such as in cosmetics, ceramics, plastics, paints, coatings and glass enamels. Thus, further investigation related to the testing stability of this nanometric $Ce_{0.95}Er_{0.05}O_{2-\delta}$ and $Ce_{0.95}Pr_{0.05}O_{2-\delta}$ compounds in real samples, such as ceramics or glass, should be done. Anyhow, the results obtained in this work will pave the way for the potential alternative to the toxic pink and red pigments widely used.

**Acknowledgement:** This work was supported by the Serbian Ministry of Education, Science, and Technological Development through the projects III 45012, III 45001, III 45007 and 172015.

## References

1. R.P. Prabhakar, M.L.P. Reddy, "Synthesis and characterisation of $(BiRE)_2O_3$ (RE: Y, Ce) pigments", *Dyes Pigments*, **63** (2004) 169–174.
2. M. Jansen, H.P. Letschert, "Inorganic yellow-red pigments without toxic metals", *Nature*, **404** (2000) 980–982.
3. R. Olazcuaga, G.L. Polles, A.E. Kira, G.L. Flem, P. Maestro, "Optical properties of $Ce_{1-x}Pr_xO_2$ powders and their applications to the coloring of ceramics", *J. Solid State Chem.*, **71** (1987) 570–573.
4. N. Maso, H. Beltran, R. Munoz, B. Julian, J.B. Carda, P. Escribano, E. Cordoncillo, "Optimization of praseodymium-doped cerium pigment synthesis temperature", *J. Am. Ceram. Soc.*, **86** (2003) 425–430.
5. D.R. Swiler, *Inorganic Pigments*, in: *Kirk-Othmer Encyclopedia of Chem. Technol.*, 5th ed., Wiley and Sons, Inc. New York, 2006.
6. R.P. Prabhakar, M.L.P. Reddy, "$(TiO_2)_1(CeO_2)_{1-x}(RE_2O_3)_x$ – novel environmental secure pigments", *Dyes Pigments*, **73** (2007) 292–297.
7. S. Furukawa, T. Masui, N. Imanaka, "New environment-friendly yellow pigments based on $CeO_2$-$ZrO_2$ solid solutions", *J. Alloys Compd.*, **451** (2008) 640–643.
8. N. Khichar, S. Bishnoi, S. Chawla, "Introducing dual excitation and tunable dual emission in ZnO through selective lanthanide ($Er^{3+}$/$Ho^{3+}$) doping", *RSC Adv.*, **4** (2014) 18811–18817.
9. H. Li, Y. Jia, W. Sun, R. Zhao, J. Fu, J. Jiang, S. Zhang, R. Pang, C. Li, "Novel energy transfer mechanism in single-phased color-tunable $Sr_2CeO_4$:$Eu^{3+}$ phosphors for WLEDs", *Optical Mater.*, **36** (2014) 1883–1889.
10. E.M. Lemdek, K. Benkhouja, S. Touhtouh, K. Sbiaai, A. Arbaoui, M. Bakasse, A. Hajjaji, Y. Boughaleb, R. Saez-Puche, "Influence of $Ca^{2+}$ doped on structural and optical properties of $RPO_4$ (R = $Ce^{3+}$, $Nd^{3+}$ and $Pr^{3+}$) compounds", *Optical Mater.*, **36** (2013) 86–90.
11. G. Gheno, M. Bortoluzzi, R. Ganzerla, F. Enrichi, "Inorganic pigments doped with tris(pyrazol-1-yl)borate lanthanide complexes: A photoluminescence study", *J. Luminesc.*, **145** (2014) 963–969.
12. M. Stojmenović, M.C. Milenković, P.T. Banković, M. Žunić, J.J. Gulicovski, J.R., Pantić, S.B. Bošković, "Influence of temperature and dopant concentration on structural, morphological and optical properties of nanometric $Ce_{1-x}Er_xO_{2-\delta}$ (x = 0.05–0.20) as a pigment", *Dyes Pigments*, **123** (2015) 116–124.
13. S. Tnunekawa, J.T. Wang, Y. Kawazoe, A. Kasuya, "Blueshifts in the ultraviolet absorption spectra of cerium oxide nanocrystallites", *J. Appl. Phys.*, **94** (2003) 3654–3656.
14. S.T. Aruna, S. Ghosk, K.C. Patil, "Combustion synthesis and properties of $Ce_{1-x}Pr_xO_{2-\delta}$ red ceramic pigments", *Int. J. Inorg. Mater.*, **3** (2001) 387–392.
15. S.F. Santos, M.C. De Andrade, J.A. Sampaio, A.B. Luz, T. Ogasawara, "Synthesis of ceria-praseodymia pigments by citrate-gel method for dental restorations", *Dyes Pigments*, **75** (2007) 574–579.
16. R.A. Eppler, "Solid state reactions in the preparation of zircon stains", pp. 1021–1045 in *Physics of Electronic Materials, Part B*, Eds. L.L. Hench, D.B. Dove, Marcel Dekker, New York, 1972.
17. T. Masui, S. Furukawa, N. Imanaka, "Synthesis and characterization of $CeO_2$-$ZrO_2$-$Bi_2O_3$ solid solutions for environment-friendly yellow pigments", *Chem. Lett.*, **35** (2006) 1032–1033.
18. B. Matovic, S. Boskovic, M. Logar, M. Radovic, Z. Dohcevic-Mitrovic, Z.V. Popovic, F. Aldinger, "Synthesis and characterization of the nanometric Pr-doped ceria", *J. Alloys Compd.*, **505** (2010) 235–238.
19. A A.I.Y. Tok, F.Y.C. Boey, Z. Dong, X.L. Sun, "Hydrothermal synthesis of $CeO_2$ nanoparticles", *J. Mater. Process. Technol.*, **190** (2007) 217–222.
20. M. Lipińska-Chwałek, F. Schulze-Küppers, J. Malzbender, "Mechanical properties of pure and doped cerium oxide", *J. Eur. Ceram. Soc.*, **35** (2015) 1539–1547.
21. S. Phoka, P. Laokul, E. Swatsitang, V. Promarack, "Synthesis, structural and optical properties of $CeO_2$ nanoparticles synthesized by a simple polyvinyl pyrrolidone (PVP) solution route", *Mater. Chem. Phys.*, **115** (2009) 423–428.
22. M.J. Godinho, R.F. Goncalvez, L.P.S. Santos, J.A. Varela, E. Longo, E.R. Leite, "Room temperature co-precipitation of nanocrystalline $CeO_2$ and $Ce_{0.8}Gd_{0.2}O_{1.9-\delta}$ powder", *Mater. Lett.*, **61** (2007) 1904–1907.
23. M. Stojmenović, S. Bošković, S. Zec, B. Babić, B. Matović, D. Bučevac, Z. Dohčević-Mitrović, F. Aldinger, "Characterization of nanometric multidoped ceria powders", *J. Alloy. Compd.*, **507** (2010) 279–285.
24. N. Paunović, Z. Dohčević-Mitrović, R. Scurtu, S. Škrabić, M. Prekajski, B. Matović, Z.V. Popović, "Suppression of inherent ferromagnetism in Pr-doped $CeO_2$ nanocrystals",

*Nanoscale*, **4** (2012) 5469–5476.
25. M. Stojmenović, M.C. Pagnacco, V. Dodevski, J. Gulicovski, M. Žunić, S. Bošković, "Studies on structural and morphological properties of multidoped ceria $Ce_{0.8}Nd_{0.0025}Sm_{0.0025}Gd_{0.005}Dy_{0.095}Y_{0.095}O_{2-\delta}$ (x = 0.2) as solid solutions", *J. Spectroscopy*, **2016** (2016) 5184542.
26. M. Stojmenović, S. Bošković, M. Žunić, B. Babić, B. Matović, D. Bajuk-Bogdanović, S. Mentus, "Studies on structural, morphological and electrical properties of $Ce_{1-x}Er_xO_{2-\delta}$ (x = 0.05–0.20) as solid electrolyte for IT-SOFC", *Mater. Chem. Phys.*, **153** (2015) 422–431.
27. M. Stojmenović, M. Žunić, J. Gulicovski, V. Dodevski, M. Prekajski, A. Radulović, S. Mentus, "Structural, morphological and electrical properties of $Ce_{1-x}Ru_xO_{2-\delta}$ (x = 0.005–0.02) solid solutions", *Ceram. Int.*, **42** (2016) 14011–14020.
28. W. Kaewwiset, K. Thamaphat, J. Kaewkhao, P. Limsuwan, "$Er^{3+}$-doped soda-lime silicate glass: artificial pink gemstone", *Am. J. App. Sci.*, **9** (2012) 1769–1775.
29. A.R. Jha, *Rare Earth Materials: Properties and Applications*, CRC Press Taylor & Francis Group, 2014.
30. S.J. Hong, A.V. Virkar, "Lattice parameters and densities of rare earth oxide doped ceria electrolytes", *J. Am. Ceram. Soc.*, **78** (1995) 433–439.
31. W. Hall, G.K. Williamson, "X-ray line broadening from filed Al and W", *Acta Metal.*, **1** (1953) 22–31.
32. R.D. Shannon, "Revised effective ionic radii and systematic studies of interatomic distances in halides and chalcogenides", *Acta Crystallogr.*, **A32** (1976) 751–767.
33. L. Wu, H.J. Wiesmann, A.R. Moodenbaugh, R.F. Klie, Y. Zhu, D.O. Welch, M. Suenaga, "Oxidation state and lattice expansion of $CeO_{2-x}$ nanoparticles as a function of particle size", *Phys. Rev. B*, **69** (2004) 125415–125416.
34. S. Tsunekawa, S. Ito, Y. Kawazoe, "Surface structures of cerium oxide nanocrystalline particles from the size dependence of the lattice parameters", *Appl. Phys. Lett.*, **85** (2004) 3845–3847.
35. S. Lütkehoff, M. Neumann, A. Ślebarski, "3d and 4d x-ray-photoelectron spectra of Pr under gradual oxidation", *Phys. Rev. B: Condens. Matter*, **52** (1995) 13808–13811.
36. M.Y. Sinev, G.W. Graham, L.P. Haack, M. Shelef, "Kinetic and structural studies of oxygen availability of the mixed oxides $Pr_{1-x}M_xO_y$ (M = Ce, Zr)", *J. Mater. Res.*, **11** (1996) 1960–1971.
37. S. Aškrabić, Z. Dohčević-Mitrović, A. Kremenović, N. Lazarević, V. Kahlenberg, Z.V. Popović, "Oxygen vacancy-induced microstructural changes of annealed $CeO_{2-x}$ nanocrystals", *J. Raman Spectrosc.*, **43** (2014) 76–81.
38. D. Andreescu, E. Matijevic, D.V. Goia, "Formation of uniform colloidal ceria in polyol", *Colloids. Surf. A*, **291** (2006) 93–100.
39. J. Liu, Z. Zhao, J. Wang, C. Xu, A. Duan, G. Jiang, Q. Yang, "The highly active catalysts of nanometric $CeO_2$-supported cobalt oxides for soot combustion", *Appl. Catal. B*, **84** (2008) 185–195.
40. S. Wang, F. Gu, C. Li, H. Cao, "Shape-controlled synthesis of $CeOHCO_3$ and $CeO_2$ microstructures", *J. Cryst. Growth*, **307** (2007) 386–394.
41. Y. Xijuan, X. Pingbo, S. Qingde, "Size-dependent optical properties of nanocrystalline $CeO_2$:Er obtained by combustion synthesis", *Phys. Chem. Chem. Phys.*, **3** (2001) 5266–5269.
42. A. Sharma, M. Varshney, J. Park, T.K. Ha, K.H. Chae, H.J. Shin, "Bifunctional $Ce_{1-x}Er_xO_2$ ($0 \le x \le 0.3$) nanoparticles for photoluminescence and photocatalyst applications: An X-ray absorption spectroscopy study", *Phys. Chem. Chem. Phys.*, **17** (2015) 30065–30075.
43. S.A. Ansari, M.M. Khan, M.O. Ansari, S. Kalathil, J. Lee, M.H. Cho, "Band gap engineering of $CeO_2$ nanostructure using an electrochemically active bio film for visible light applications", *RSC Adv.*, **32** (2014) 16782–16791.
44. J. Tauc, R. Grigorovici, A. Vancu, "Optical properties and electronic structure of amorphous germanium", *Phys. Status Solidi*, **15** (1966) 627–637.
45. L.S. Cavalcante, V.M. Longo, J.C. Sczancoski, M.A.P. Almeida, A.A. Batista, J.A. Varela, M.O. Orlandi, E. Longo, M.S. Li, "Electronic structure, growth mechanism and photoluminescence of $CaWO_4$ crystals", *Cryst. Eng. Comm.*, **14** (2012) 853–868.